



Article

Capacitive Properties of Ferrimagnetic NiFe₂O₄-Conductive Polypyrrole Nanocomposites

Michael MacDonald and Igor Zhitomirsky *

Department of Materials Science and Engineering, McMaster University, Hamilton, ON L8S 4L7, Canada;
macdom45@mcmaster.ca

* Correspondence: zhitom@mcmaster.ca

Abstract: This investigation addresses increasing interest in advanced composite materials, combining capacitive properties and spontaneous magnetization for energy storage applications in supercapacitors. The capacitive properties of ferrimagnetic NiFe₂O₄ (NFO) spinel nanoparticles with magnetization of 30 emu g⁻¹ were enhanced using high-energy ball-milling and the use of advanced dispersant, which facilitated charge transfer. NFO electrodes with an active mass of 40 mg cm⁻² showed a capacitance of 1.46 F cm⁻² in 0.5 M Na₂SO₄ electrolyte in a negative potential range. The charging mechanism in the negative potential range in Na₂SO₄ electrolyte was proposed. NFO was combined with conductive polypyrrole polymer for the fabrication of composites. The analysis of the capacitive behavior of the composites using cyclic voltammetry, chronopotentiometry and impedance spectroscopy at different electrode potentials revealed synergy of contributions of NFO and PPy. The highest capacitance of 6.64 F cm⁻² was obtained from cyclic voltammetry data. The capacitance, impedance, and magnetic properties can be varied by variation of electrode composition. Composite electrodes are promising for application in anodes of asymmetric magnetic supercapacitors for energy storage and magnetically enhanced capacitive water purification devices.

Keywords: supercapacitor; ferrite; polypyrrole; composite; capacitance



Citation: MacDonald, M.; Zhitomirsky, I. Capacitive Properties of Ferrimagnetic NiFe₂O₄-Conductive Polypyrrole Nanocomposites. *J. Compos. Sci.* **2024**, *8*, 51. <https://doi.org/10.3390/jcs8020051>

Academic Editor: Kyong Yop Rhee

Received: 23 December 2023

Revised: 13 January 2024

Accepted: 26 January 2024

Published: 30 January 2024



Copyright: © 2024 by the authors. Licensee MDPI, Basel, Switzerland. This article is an open access article distributed under the terms and conditions of the Creative Commons Attribution (CC BY) license (<https://creativecommons.org/licenses/by/4.0/>).

1. Introduction

Conductive polymers have generated significant interest for the fabrication of composites, combining various functional properties of individual components. Polyaniline (PANI)- and polypyrrole (PPy)-based composites containing magnetic particles have been developed [1–3]. These composite materials have shown interesting properties, which result from the interfacial interactions of magnetic particles and conductive polymers. PANI-coated ferromagnetic particles showed enhanced magnetoresistance [4] due to the spin-polarized tunneling of electrons between grains of the ferromagnetic material, which was facilitated by the conducting electrons of the polymer [4]. Surface modification of a ferromagnetic material with PPy resulted in significant magnetization increase [3]. In such composites, the measured magnetic moment of Mn ions was higher than theoretically expected. The magnetization increase resulted from spin and charge transfer from the conductive polymer to the magnetic material. It was suggested [3] that the π electrons of PPy are polarized in exchange interactions with 3D electrons of Mn ions, resulting in an increase in the total magnetic moment.

There is currently a surge of interest in composites containing conductive polymers [5–9] for application in supercapacitors. It has been reported that the capacitance of PPy composites containing ferromagnetic lanthanum strontium manganate nanoparticles is higher than the capacitance of pure PPy electrodes [10]. Composite materials containing polypyrrole and magnetic particles are scientifically and technologically fascinating. Such composites are promising for energy storage and capacitive deionization of water applications.

NiFe_2O_4 (NFO) is a promising ferrimagnetic spinel material for the development of magnetic supercapacitor composites with PPy. Many investigations [11–15] tested capacitive properties of NFO and composites in positive potential windows in KOH electrolyte. Good capacitive properties in KOH electrolyte were reported in a relatively small potential window of ~0.4–0.5 V [16–20]. The tested electrodes had a relatively low active mass, typically below 5 mg cm^{-2} . Significantly higher active mass loadings are required for practical applications. It should be noted that PPy shows poor electrochemical performance and degradation of properties in KOH electrolyte. NFO and composites were also tested in KNO_3 [21], LiCl [22], LiClO_4 [23], and other electrolytes [24]. NFO-PPy core shell composite materials were tested in H_2SO_4 electrolyte [25]. However, the use of acidic H_2SO_4 electrolyte can result in NFO degradation. It is hypothesized that neutral Na_2SO_4 electrolyte is beneficial for the charge storage of both PPy and NFO.

The objective of this investigation was the fabrication of NFO-PPy composites with high active mass for operation in a Na_2SO_4 electrolyte. The electric charge storage properties of NFO were enhanced using high-energy ball-milling (HEBM) and application of a dispersant-charge transfer mediator. As a result, the capacitance of NFO electrodes was higher than reported in previous investigations. The combination of NFO and PPy offers the advantages of the synergy of contributions of individual components at different electrode potentials. In contrast with previous studies, high capacitance was achieved in a negative potential range. Composite electrodes showed promising electrochemical performance and combined charge storage and ferrimagnetic properties.

2. Materials and Methods

Gallocyanine dye (GCD), Na_2SO_4 , ammonium persulfate (APS), NiFe_2O_4 (NFO, nanoparticles, <50 nm size), pyrrole, 4,5-Dihydroxy-1,3-benzenedisulfonic acid disodium salt monohydrate (Tiron), ethanol, and poly(vinyl butyral) (PVB, 200–300 kDa) were purchased from MilliporeSigma, Burlington, ON, Canada). Carbon nanotubes (CNT, multi-walled, 13 nm diameter, 1–2 μm length, Bayer, Leverkusen, Germany) and commercial Ni foam current collectors (95% porosity, 1.6 mm thickness, Vale, Mississauga, ON, Canada) were used. PPy polymerization was performed using aqueous 0.1 M pyrrole solutions containing 0.01 M Tiron; this was achieved by adding 0.1 M APS at 0 °C.

High-energy ball-milling (HEBM) of NFO was conducted using a Mixer Mill MM 500 Nano (Retsch GmbH, Haan, Germany). HEBM consisted of milling steps at a frequency of 15 Hz during 5 min with 90 s intervals between the steps. The milling duration was 2 h. After HEBM, the NFO material was washed with ethanol and dried.

NFO and CNT were co-dispersed in ethanol using GCD as a dispersant. The mass ratio of NFO–CNT was 8:2. The mass ratio (R_D) of GCD dispersant to the total mass of NFO and CNT was $R_D = 0.02\text{--}0.1$. The mixtures underwent ultrasonication, washing, and drying and re-dispersion in ethanol containing dissolved PVB binder. The obtained slurries were then utilized for electrode fabrication by impregnating current collectors. PPy-CNT and PPy–NFO–CNT composite powders were also dispersed in PVB solution in ethanol. The mass ratio of PPy–NFO was 1:1 (Composite 1) and 1:3 (Composite 2). All the electrodes contained 20% CNT as conductive additives. In each electrode, the mass ratio of PVB to the total mass of NFO, PPy and CNT was 0.03. The final mass of the impregnated material, after drying, was 40 mg cm^{-2} . The impregnated Ni foams were pressed to 25% of their initial thickness.

A SQUID magnetometer (Quantum Design, San Diego, CA, USA) was used for investigation of magnetic properties. XRD testing was conducted with a diffractometer Bruker D8 Advance with Cr- $K\alpha$ radiation. The microstructure investigations involved the use of transmission electron microscopy (TEM, Talos 200 microscope, Thermo Scientific, Waltham, MA, USA). Electrochemical characterization was carried out in aqueous 0.5 M Na_2SO_4 electrolyte using a Biologic potentiostat (VMP 300, BioLogic, Seyssinet-Pariset, France) with a three-electrode system, using a saturated calomel electrode reference (SCE), an NFO-based working electrode, and a Pt mesh counter electrode. Cyclic voltammetry (CV),

electrochemical impedance spectroscopy (EIS), and chronopotentiometry (CP) methods were used for electrode characterization. The capacitance was calculated from the CV, EIS and CP data as described in Ref. [26]. Areal (C_S) and gravimetric (C_m) capacitances were derived from the CV data using the following equation:

$$C = \frac{\Delta Q}{\Delta U} = \frac{\left| \int_0^{t(U_{max})} I dt \right| + \left| \int_{t(U_{max})}^0 I dt \right|}{2U_{max}} \quad (1)$$

where ΔQ is charge, I is current, t is time, ΔU is potential range, and from the CP data,

$$C = I\Delta t / \Delta U \quad (2)$$

The complex capacitance $C^*(\omega) = C'(\omega) - iC''(\omega)$ was derived at different frequencies (ω) from the complex impedance $Z^*(\omega) = Z'(\omega) + iZ''(\omega)$:

$$C'(\omega) = \frac{-Z''(\omega)}{\omega Z(\omega)^2} \quad (3)$$

$$C''(\omega) = \frac{Z'(\omega)}{\omega Z(\omega)^2} \quad (4)$$

3. Results

NFO showed soft ferrimagnetic properties with spontaneous magnetization of 30 emu g⁻¹ and a small coercive field (Figure 1). The obtained magnetization value is in agreement with data from the literature [27]. However, the magnetization of NFO is dependent on particle size, temperature, distribution of Ni²⁺ and Fe³⁺ ions in the tetrahedral and octahedral positions of the spinel crystalline structure and other factors [28–30].

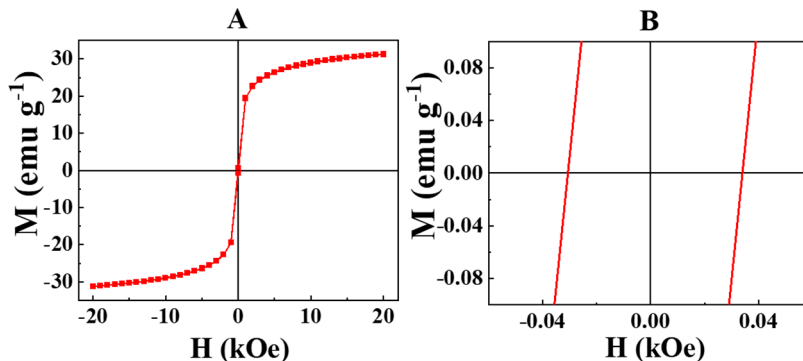


Figure 1. (A) Magnetization (M) versus magnetic field (H) and (B) M versus H in the low H range.

The size of the NFO particles was analyzed using TEM. The as-received NFO particles (Figure 2A, Supplementary Information, Figure S1) showed well-defined crystal faces. The typical particle size was 20–40 nm in agreement with the data of powder manufacturer. The investigation of morphology of HEBM powders showed particles of irregular shapes which resulted from particle grinding (Figure 2B). The typical particle size was below 20 nm and the powders contained many particles with sizes below 10 nm. It was hypothesized that particle size reduction can be beneficial for obtaining electrodes with higher capacitance. However, it should be noted that other investigations of different materials did not show correlation between electrochemical capacitance and BET surface area [31–33].

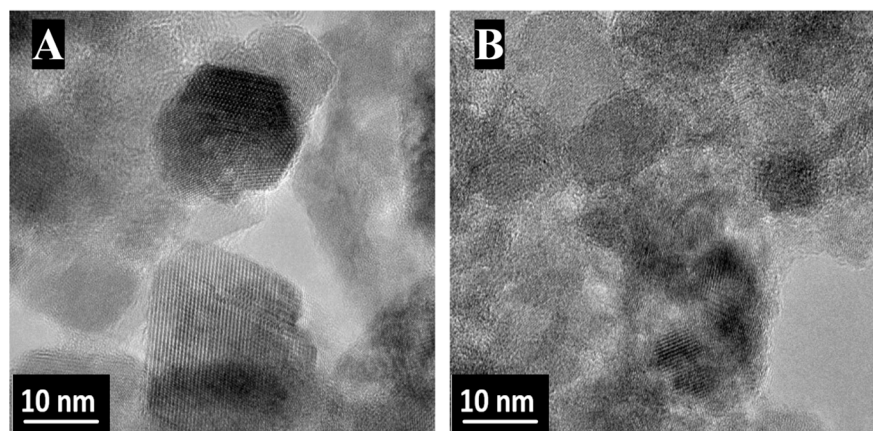


Figure 2. TEM images of (A) as-received and (B) HEBM NFO.

Figures 3 and S2–S4 compare electrochemical testing results for as-received NFO and HEBM NFO prepared with and without GCD. The CV data for as-received NFO (Figure 3A(a)) showed a reduction in current with increasing potential from -0.8 to 0 V, which indicated decreasing differential capacitance at higher potentials. The use of GCD as a dispersant for the NFO particles led to significant changes in CV shape (Figure 3A(b)) for $R_D = 0.02$. The NFO electrodes prepared with GCD showed a significant increase in current in the potential range of -0.6 – 0 V, and redox peaks were observed at about -0.2 V. It was found that the increase in R_D from 0.02 to 0.1 did not result in significant changes in CV shape (Figure S2). The changes in CV shape can be attributed to the effect of adsorbed GCD. It is suggested that for $R_D = 0.02$, only part of GCD adsorbed on NFO and non-adsorbed GCD was removed during washing. Further addition of GCD ($0.02 < R_D \leq 0.1$) did not result in higher capacitance. The NFO electrodes, prepared without and with GCD ($R_D = 0.02$) showed capacitances of 0.55 and 0.91 F cm $^{-2}$, respectively, at 2 mV s $^{-1}$. HEBM NFO showed significantly higher currents, especially for potentials above -0.6 V (Figure 3B(a)).

The use of GCD ($R_D = 0.02$) resulted in a further increase in currents for potentials above -0.4 V. Redox peaks were also observed for the electrode prepared with GCD dispersant (Figure 3B(b)). The HEBM NFO electrodes prepared without and with GCD showed capacitances of 1.32 and 1.46 F cm $^{-2}$, respectively, at 2 mV s $^{-1}$. The analysis of dependences of capacitance versus sweep rate (Figure 3C) showed that the use of GCD and HEBM resulted in improved capacitive properties in the range of 2 – 100 mV s $^{-1}$. The use of GCD for HEBM NFO resulted in improved capacitive properties at low sweep rates below 20 mV s $^{-1}$. However, at higher sweep rates the use of GCD for HEBM resulted in reduced capacitance. CP testing results showed that the use of GCD for as-prepared NFO and HEBM resulted in longer charge–discharge times (Figure 3D,E), which led to higher capacitances at different current densities (Figure 3F). However, the use of GCD for HEBM samples did not result in enhanced capacitance (Figure 3E,F).

GCD (Figure 4A) belongs to catechol family of molecules, which exhibit strong adsorption on inorganic particles by complexation of surface metal atoms. The adsorption mechanism of catecholate molecules is similar to that of mussel protein bonding to different surfaces by the catechol groups of the individual monomers. GCD can be adsorbed on NFO particles by complexation of Ni or Fe atoms (Figure 4B). GCD is a polyaromatic molecule (Figure 4A). Polyaromatic molecules show adsorption on CNT by π - π interactions. The positive charge of GCD is beneficial for application of this molecule as a dispersant for electrostatic stabilization of particles in suspensions. It is known that charged polyaromatic catecholates can be used as dispersants for inorganic particles and CNT. Therefore, it was hypothesized that GCD adsorbed on NFO and CNT, acting as a co-dispersant for both materials. Therefore, enhanced capacitance of electrodes prepared using GCD can result from better mixing of NFO with conducting CNT additives. It is also known that catechol

molecules can facilitate charge transfer. For example, Tiron and other anionic catechol molecules facilitated anodic electropolymerization of polypyrrole on non-noble substrates acting as charge transfer mediators, which reduce electropolymerization potential [34,35]. The use of dopamine as a charge transfer mediator facilitated the fabrication of photovoltaic devices with enhanced efficiency [36]. GCD was used as a charge transfer mediator for advanced electrochemical sensors [37].

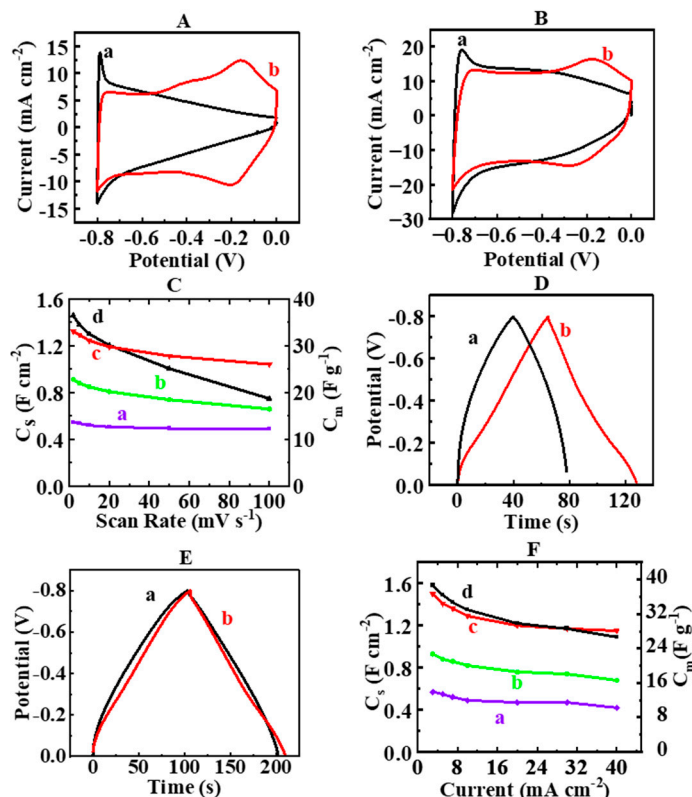


Figure 3. (A,B) CVs at 10 mV s^{-1} ; (C) capacitance calculated from CV data versus sweep rate; (D,E) CP data at 10 mA cm^{-2} ; (F) capacitance calculated from CP data versus current density for electrodes prepared using (A(a)), (C(a)), (D(a)), (F(a)) as-received NFO; (A(b)), (C(b)), (D(b)), (F(b)) as-received NFO with GCD for $R_D = 0.02$; (B(a)), (C(c)), (E(a)), (F(c)) HEBM NFO; and (B(b)), (C(d)), (E(b)), (F(d)) HEBM NFO with GCD for $R_D = 0.02$.

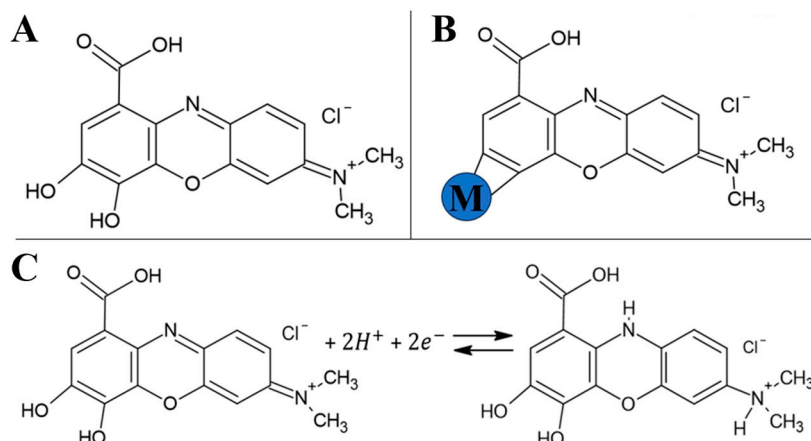
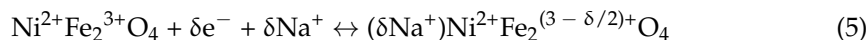


Figure 4. (A) Chemical structure of GCD; (B) adsorption of GCD on NFO involving catecholate-type bonding to surface atoms ($M = \text{Ni}, \text{Fe}$); (C) redox reaction of GCD.

It is suggested that GCD can potentially facilitate charge storage reactions of NFO. It is in this regard that GCD is a redox active molecule (Figure 4C). The mass normalized capacitance of GCD is low due to the large molecular mass of this molecule. Therefore, due to the low gravimetric capacitance and low amount of GCD adsorbed, the direct contribution of GCD to the electrode capacitance is negligible. However, GCD can act as charge transfer mediator for NFO. The charge storage mechanism of NFO in the negative potential range can be described by the following equation:



EIS data were obtained at different electrode potentials, such as 0, −0.2, −0.4, −0.6 and −0.8 V, versus SCE. Figure 5 presents EIS data for NFO and HEBM NFO electrodes prepared without and with GCD. The Nyquists plots (Figure 5A) for as-received NFO prepared without GCD showed significant differences in components of complex impedance $Z^* = Z' + iZ''$ at different electrode potentials. The highest Z^* values were obtained for potentials of 0 V and −0.2 V versus SCE, which indicated low capacitance and high electrical resistance. The NFO electrodes prepared using GCD (Figure 5B) showed reduced values of Z' and Z'' at −0.4 V. HEBM resulted in a reduced imaginary component of Z^* , which indicated an increase in differential capacitance (Figure 5C). However, the HEBM NFO electrodes showed higher resistance $R = Z'$ at all the electrode potentials. The HEBM NFO electrodes (Figure 5D) prepared using GCD showed the lowest values of $R = Z'$ and highest slopes of the Nyquist plots, which indicated improved capacitive behavior.

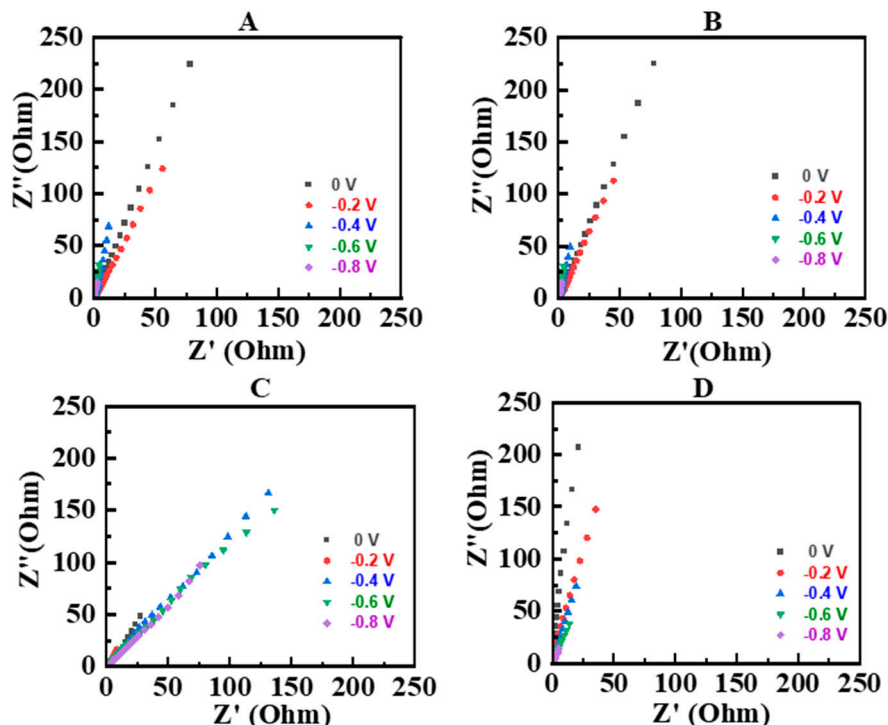


Figure 5. Nyquist plots of EIS data at different potentials for electrodes prepared using (A), as-received NFO, (B) as-received NFO with GCD for $R_D = 0.02$, (C) HEBM NFO, and (D) HEBM NFO with GCD for $R_D = 0.02$.

The HEBM NFO prepared using GCD was used for the fabrication of composites with PPy, which allowed for further improvement in properties. Figure 6 shows electrochemical testing results for PPy electrodes, containing 20% CNT. CV data (Figure 6A) showed higher currents and a wider CV area for potentials of −0.4–0 V vs. SCE, compared to the potential range of −0.8–−0.4 V vs. SCE. This is in contrast to the data for NFO electrodes, which showed higher currents in the low potential range. Therefore, the combination of PPy and

NFO is promising for overcoming disadvantages of both materials in different potential ranges. The capacitance of PPy electrodes (Figure 6B) was found to be 6.64 F cm^{-2} at 2 mV s^{-1} . However, it sharply reduced to the level of 4.4 F cm^{-2} at 10 mV s^{-1} . The electrodes showed a capacitance of 2.6 F cm^{-2} at 100 mV s^{-1} .

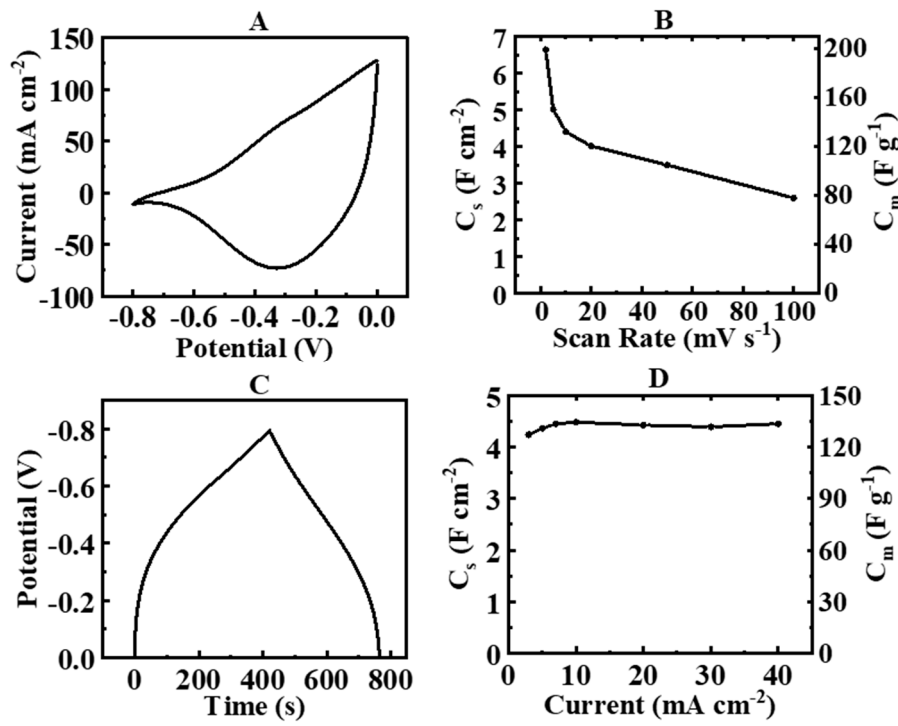
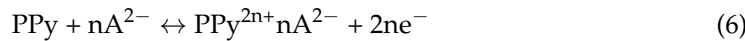


Figure 6. (A) CV at 10 mV s^{-1} , (B) capacitance derived from CVs versus sweep rate, (C) CP data at 10 mA cm^{-2} , (D) capacitance derived from CP data versus current density for PPy electrode.

The pseudocapacitive charge storage mechanism of PPy, doped with anions is given by the following equation [38,39]:



where A^{2-} is Tiron $^{2-}$ or SO_4^{2-} .

The CP data (Figure 6C) showed a deviation from linear charge–discharge potential–time dependences at constant current densities. The capacitance of 4.2 F cm^{-2} was obtained at 3 mA cm^{-2} , and relatively small variations in capacitance were observed in the range of $3\text{--}40 \text{ mA cm}^{-2}$ (Figure 6D).

HEBM NFO prepared using GCD ($R_D = 0.02$) and PPy were used for the fabrication of composites, combining ferrimagnetic and capacitive properties. The formation of composites was confirmed by X-ray diffraction studies (Figure S5). Figures 7, S6 and S7 show electrochemical testing results for Composite 1, containing NFO and PPy in a mass ratio of 1:1. The CV deviated from an ideal rectangular shape. However, reduced variations in current (Figure 7A) were observed in the potential range $-0.8\text{--}0 \text{ V}$, compared to the PPy electrode (Figure 6A). The Composite 1 electrodes exhibited capacitances of 3.86 and 1.39 F cm^{-2} at sweep rates of 2 and 100 mV s^{-1} , respectively (Figure 7B). Figure 7C,D shows CP data. The capacitance calculated from the CP data was found to be 4.22 and 3.58 F cm^{-2} for current densities of 3 and 40 mA cm^{-2} , respectively.

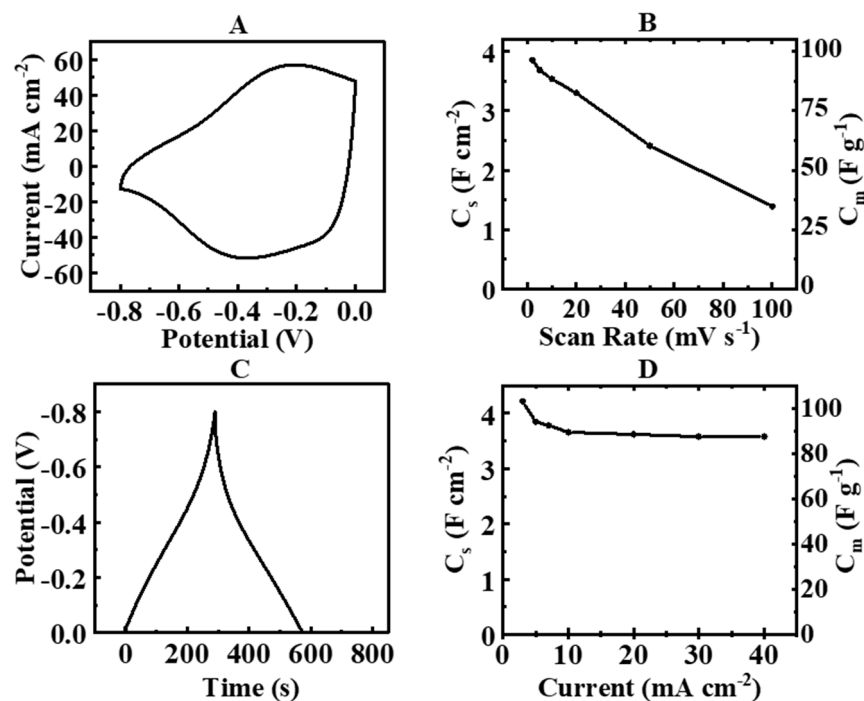


Figure 7. (A) CV at 10 mV s^{-1} , (B) capacitance derived from CVs versus sweep rate, (C) CP data at 10 mA cm^{-2} , (D) capacitance derived from CP data versus current density for Composite 1 electrode.

The capacitance for the Composite 1 electrode, calculated from the CP data, was comparable with the capacitance of PPy electrodes, despite the 50% lower PPy content and lower capacitance of NFO compared to PPy. This indicated a synergy of contributions of the individual components. The capacitance of the composite materials involves the contributions of the individual components. The corresponding charging mechanisms are described by Equations (5) and (6). It is known [26] that mass normalized capacitance usually decreases with increasing electrode mass due to limited electronic and ionic conductivities. As a result, high gravimetric capacitance is usually observed only in thin films with mass below $0.1\text{--}1.0 \text{ mg cm}^{-2}$. The mass loading increase to the level of $10\text{--}50 \text{ mg cm}^{-2}$ often results in reduction of the gravimetric capacitance by 2–3 orders of magnitude [26]. Therefore, it is challenging to utilize the capacitive properties of materials at high active mass loadings and achieve high areal capacitance. Special techniques are currently under development for the fabrication of electrodes with high active mass loadings, such as the use of coated particles, agglomerate-free processing using advanced dispersants, and liquid–liquid extraction techniques [26]. The combination of PPy and NFO is promising for the fabrication of advanced electrodes with high active mass loading. Conductive PPy improves the electronic conductivity of the composite materials and allows for better utilization of the capacitive properties of NFO. The use of ferrimagnetic NFO can facilitate electrolyte transfer via the magnetohydrodynamic effect [40], which is governed by the Lorentz force acting on the ions in the local magnetic field of the ferrimagnetic NFO particles. The magnetohydrodynamic effect can result in better utilization of capacitive properties of PPy in the bulk electrodes. This can explain the synergy of contribution of PPy and NFO.

Figure 8 presents testing results for Composite 2 with an NFO–PPy mass ratio of 3:1. The analysis of CV and CP data showed lower capacitances compared to the corresponding data for Composite 2. The capacitance calculated from the CV data decreased from 2.53 F cm^{-2} to 1.69 F cm^{-2} with an increasing sweep rate from 2 to 100 mV s^{-1} . CP data showed capacitances of 2.54 F cm^{-2} and 2.00 F cm^{-2} for current densities of 3 and 40 mA cm^{-2} , respectively. It should be noted that Composite 2 had a higher content of ferrimagnetic NFO compared

to Composite 2. Therefore, the capacitive and magnetic properties of NFO-PPy composites can be varied.

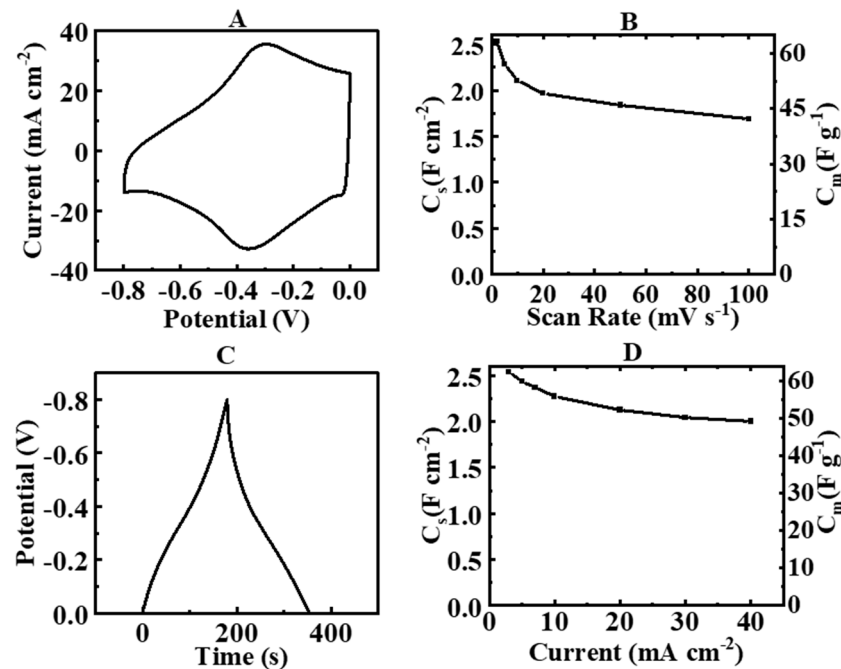


Figure 8. (A) CV at 10 mV s^{-1} , (B) capacitance derived from CVs versus sweep rate, (C) CP data at 10 mA cm^{-2} , (D) capacitance derived from CP data versus current density for Composite 2 electrode.

The EIS data for PPy, Composite 1 and Composite 2 electrodes are summarized in Figure 9. PPy electrodes showed significant differences in impedance at different electrode potentials. Relatively high values of real and imaginary parts of the complex impedance at -0.8 V indicated low differential capacitance in agreement with CV data and high resistance. However, low impedance was observed at higher potentials. Composite 1 showed significant reduction of impedance at -0.8 V . The reduction of the imaginary part indicated an increase in the differential capacitance. The decrease in the real part is attributed to the reduction in resistance. However, the electrodes showed increased resistance at -0.6 V . The EIS data were analyzed using an equivalent circuit developed for high active mass composite electrodes [41]. It included an R–C (Q) transmission line with double-layer capacitance, pseudocapacitance, Warburg impedance, solution resistance and charge transfer resistance (Figure S8). High-energy ball-milling resulted in increasing Warburg impedance. It is suggested that particle size reduction resulted in better packing of the particles, reduced porosity, and an increase in the bulk density of the electrodes. This can result in diffusion limitations and larger Warburg impedance. PPy electrodes showed significant Warburg impedance at an electrode potential of -0.8 V . The addition of NFO resulted in reduced Warburg impedance of Composites 1 and 2. The larger NFO content in the Composite 2 compared to the Composite 1 allowed for lower Warburg impedance. This can result from the magnetohydrodynamic effect of the ferrimagnetic particles. As pointed out above, such an effect facilitates electrolyte diffusion [40].

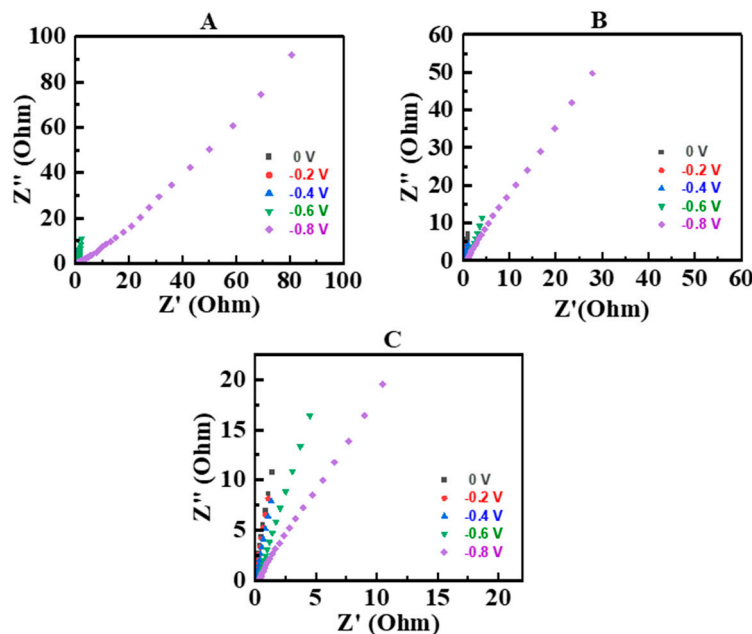


Figure 9. EIS data presented in Nyquist plots at different electrode potentials for (A) PPy, (B) Composite 1 and (C) Composite 2 electrodes.

Composite 2 showed a significant reduction in impedance at -0.8 V , compared to PPy and Composite 1. Increased impedance was observed at -0.6 and -0.4 V . It should be noted that Composites 1 and 2 showed significantly lower impedance values at potentials of -0.2 and 0 V , compared to NFO. In general, Composites 1 and 2 showed reduced variations in impedance in the potential range of $-0.8\text{--}0\text{ V}$, which illustrate the benefits of the composite materials compared to the individual components.

Figure 10 shows the capacitance retention of Composite 1, which exhibited higher capacitance compared to Composite 2. The initial increase in capacitance during the first 100 cycles can be attributed to different factors, such as changes in the microstructure of the bulk of the electrode or improved wetting of the electrode by the electrolyte. The capacitance retention after 1000 cycles was found to be 93.5%. It should be noted that HEBM NFO electrodes showed a slight reduction in capacitance during the first 50 cycles, and then capacitance increased. The capacitance retention after 1000 cycles was found to be 103.5% (Figure S9).

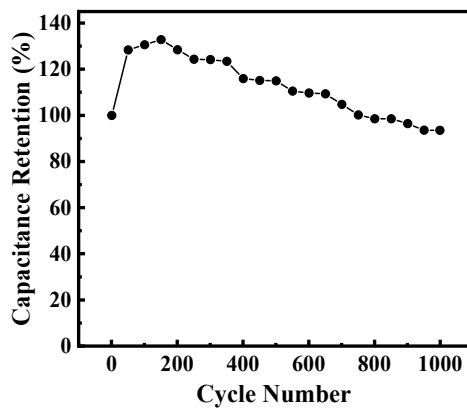


Figure 10. Capacitance retention of the Composite 1 electrode.

Composites 1 and 2 combine capacitive and ferrimagnetic properties, which are promising for novel applications based on magnetocapacitive phenomena. Such phenomena are currently under intensive investigation in various magnetically ordered pseu-

docapacitive materials [40]. Composites 1 and 2 are promising for energy storage in supercapacitors and magnetic capacitive water deionization devices.

4. Conclusions

NFO nanoparticles showed magnetization of 30 emu g^{-1} and capacitive properties in $0.5 \text{ M Na}_2\text{SO}_4$ electrolyte in a negative potential range. The capacitive properties of NFO can be increased significantly using HEBM and GCD, which acted as a dispersant and charge transfer mediator. The NFO electrodes with high active mass loading of 40 mg cm^{-2} showed a capacitance of 1.46 F cm^{-2} . The ability to achieve high capacitance of NFO was beneficial for the fabrication of PPy–NFO composites, which showed a capacitance of 6.64 F cm^{-2} . The analysis of CV, CP and EIS data at different electrode potentials showed a synergy of the contributions of the individual components to the capacitance of PPy–NFO composites. The capacitive properties, impedance, and magnetization of the composites can be varied by variation of PPy and NFO content. The high capacitance in the negative potential range in Na_2SO_4 electrolyte overcomes the problem of the lower capacitance of materials for negative electrodes compared to the capacitance of positive electrodes, such as MnO_2 . Therefore, the composite material prepared in this investigation is promising for the fabrication of asymmetric capacitors with an enlarged voltage window. The combination of capacitive and magnetic material in the composite opens an avenue for the preparation of advanced magnetically enhanced devices for energy storage and capacitive deionization of water.

Supplementary Materials: The following supporting information can be downloaded at: <https://www.mdpi.com/article/10.3390/jcs8020051/s1>, Figures S1–S9, TEM, CV, CP, XRD, equivalent circuit, capacitance retention data and related references [42,43]. Figure S1. High resolution TEM image of NFO showing (111) planes. Figure S2. CVs at 10 mV s^{-1} for NFO electrodes, prepared using as-received NFO: (a) without GCD and (b-d) with GCD for (b) $R_D=0.02$, (c) $R_D=0.05$ and (d) $R_D=0.1$. Figure S3. CVs at different sweep rates for (A) as-received NFO, (B) as-received NFO with GCD at different scan rates, (C) HEBM NFO and (D) HEBM NFO with GCD. Figure S4. CP data at different current densities for (A) as-received NFO, (B) as-received NFO with GCD at different scan rates, (C) HEBM NFO and (D) HEBM NFO with GCD. Figure S5. X-ray diffraction pattern of Composite 1. (\blacklozenge - MWCNT, JCPDS file 00-058-1638, ∇ -PPy, \bullet -NFO, JCPDS file 00-044-1485). Figure S6. CVs at different sweep rates for (A) PPy, (B) Composite 1 and (C) Composite 2 electrodes. Figure S7. CP data at different current densities for (A) PPy, (B) Composite 1 and (C) Composite 2 electrodes. Figure S8. Equivalent circuit used for EIS data simulation. Figure S9. Capacitance retention of HEBM NFO with GCD for $R_D=0.02$.

Author Contributions: Conceptualization, M.M. and I.Z.; methodology, M.M.; validation, M.M.; formal analysis, M.M.; investigation, M.M.; resources, I.Z.; data curation, M.M.; writing—original draft preparation, M.M. and I.Z.; writing—review and editing, M.M. and I.Z.; supervision, I.Z.; project administration, I.Z.; funding acquisition, I.Z. All authors have read and agreed to the published version of the manuscript.

Funding: This research was funded by the Natural Sciences and Engineering Research Council of Canada, grant number RGPIN-2018-04014, and the CRC program.

Data Availability Statement: Data contained within the article are available.

Acknowledgments: Electron microscopy investigations were performed at the Canadian Centre for Electron Microscopy.

Conflicts of Interest: The authors declare no conflicts of interest.

References

1. Romero, M.; Faccio, R.; Montenegro, B.; Tumelero, M.A.; Cid, C.C.P.; Pasa, A.A.; Mombrú, A.W. Role of conducting polyaniline interphase on the low field magnetoresistance for LSMO-PANI nanocomposites. *J. Magn. Magn. Mater.* **2018**, *466*, 446–451. [[CrossRef](#)]
2. Romero, M.; Faccio, R.; Pardo, H.; Tumelero, M.A.; Cid, C.C.P.; Pasa, A.A.; Mombrú, Á.W. Microstructure, interparticle interactions and magnetotransport of manganite-polyaniline nanocomposites. *Mater. Chem. Phys.* **2016**, *171*, 178–184. [[CrossRef](#)]

3. Pana, O.; Soran, M.; Leostean, C.; Macavei, S.; Gautron, E.; Teodorescu, C.; Gheorghe, N.; Chauvet, O. Interface charge transfer in polypyrrole coated perovskite manganite magnetic nanoparticles. *J. Appl. Phys.* **2012**, *111*, 044309. [[CrossRef](#)]
4. Gupta, K.; Jana, P.; Meikap, A.; Nath, T. Synthesis of $\text{La}_{0.67}\text{Sr}_{0.33}\text{MnO}_3$ and polyaniline nanocomposite with its electrical and magneto-transport properties. *J. Appl. Phys.* **2010**, *107*, 073704. [[CrossRef](#)]
5. Patil, P.H.; Kulkarni, V.V.; Dongale, T.D.; Jadhav, S.A. α -Manganese Dioxide ($\alpha\text{-MnO}_2$) Coated with Polyaniline (PANI) and Reduced Graphene Oxide (rGO)-Based Nanocomposite for Supercapacitor Application. *J. Compos. Sci.* **2023**, *7*, 167. [[CrossRef](#)]
6. Patil, P.H.; Kulkarni, V.V.; Jadhav, S.A. An Overview of Recent Advancements in Conducting Polymer-Metal Oxide Nanocomposites for Supercapacitor Application. *J. Compos. Sci.* **2022**, *6*, 363. [[CrossRef](#)]
7. Kausar, A.; Ahmad, I.; Zhao, T.; Aldaghri, O.; Ibnaouf, K.H.; Eisa, M.H. Cutting-Edge Graphene Nanocomposites with Polythiophene—Design, Features and Forefront Potential. *J. Compos. Sci.* **2023**, *7*, 319. [[CrossRef](#)]
8. Kausar, A.; Ahmad, I. Electrospinning Processing of Polymer/Nanocarbon Nanocomposite Nanofibers—Design, Features, and Technical Compliances. *J. Compos. Sci.* **2023**, *7*, 290. [[CrossRef](#)]
9. Wang, Y.; Wang, Y.; Wang, C.; Wang, Y. A Hierarchical Architecture of Functionalized Polyaniline/Manganese Dioxide Composite with Stable-Enhanced Electrochemical Performance. *J. Compos. Sci.* **2021**, *5*, 129. [[CrossRef](#)]
10. Amarnath, C.A.; Ghamous, F.; Schmaltz, B.; Autret-Lambert, C.; Roger, S.; Gervais, F.; Tran-Van, F. Polypyrrole/lanthanum strontium manganite oxide nanocomposites: Elaboration and characterization. *Synth. Met.* **2013**, *167*, 18–24. [[CrossRef](#)]
11. Al-Rubaye, S.; Rajagopalan, R.; Subramaniyam, C.; Tai, Z.; Xian, J.; Wang, X.; Dou, S.X.; Cheng, Z. $\text{NiFe}_{(2)}\text{O}(4)$ nanoparticles coated on 3D graphene capsule as electrode for advanced energy storage applications. *Dalton Trans.* **2018**, *47*, 14052–14059. [[CrossRef](#)]
12. Arun, T.; Kavinkumar, T.; Udayabhaskar, R.; Kiruthiga, R.; Morel, M.J.; Aepuru, R.; Dineshbabu, N.; Ravichandran, K.; Akbari-Fakhrebadi, A.; Mangalaraja, R.V. NiFe_2O_4 nanospheres with size-tunable magnetic and electrochemical properties for superior supercapacitor electrode performance. *Electrochim. Acta* **2021**, *399*, 139346. [[CrossRef](#)]
13. Askari, M.B.; Salarizadeh, P. Binary nickel ferrite oxide (NiFe_2O_4) nanoparticles coated on reduced graphene oxide as stable and high-performance asymmetric supercapacitor electrode material. *Int. J. Hydrot. Energy* **2020**, *45*, 27482–27491. [[CrossRef](#)]
14. Baig, M.M.; Pervaiz, E.; Azad, M.; Jahan, Z.; Khan Niazi, M.B.; Baig, S.M. $\text{NiFe}_2\text{O}_4/\text{SiO}_2$ nanostructures as a potential electrode material for high rated supercapacitors. *Ceram. Int.* **2021**, *47*, 12557–12566. [[CrossRef](#)]
15. Bandgar, S.B.; Vadiyar, M.M.; Ling, Y.-C.; Chang, J.-Y.; Han, S.-H.; Ghule, A.V.; Kolekar, S.S. Metal Precursor Dependent Synthesis of NiFe_2O_4 Thin Films for High-Performance Flexible Symmetric Supercapacitor. *ACS Appl. Energy Mater.* **2018**, *1*, 638–648. [[CrossRef](#)]
16. Deyab, M.A.; Awadallah, A.E.; Ahmed, H.A.; Mohsen, Q. Progress study on nickel ferrite alloy-graphene nanosheets nanocomposites as supercapacitor electrodes. *J. Energy Storage* **2022**, *46*, 103926. [[CrossRef](#)]
17. Gao, X.; Bi, J.; Wang, W.; Liu, H.; Chen, Y.; Hao, X.; Sun, X.; Liu, R. Morphology-controllable synthesis of NiFe_2O_4 growing on graphene nanosheets as advanced electrode material for high performance supercapacitors. *J. Alloys Compd.* **2020**, *826*, 154088. [[CrossRef](#)]
18. Gao, X.; Wang, W.; Bi, J.; Chen, Y.; Hao, X.; Sun, X.; Zhang, J. Morphology-controllable preparation of NiFe_2O_4 as high performance electrode material for supercapacitor. *Electrochim. Acta* **2019**, *296*, 181–189. [[CrossRef](#)]
19. Hua, M.; Xu, L.; Cui, F.; Lian, J.; Huang, Y.; Bao, J.; Qiu, J.; Xu, Y.; Xu, H.; Zhao, Y.; et al. Hexamethylenetetramine-assisted hydrothermal synthesis of octahedral nickel ferrite oxide nanocrystallines with excellent supercapacitive performance. *J. Mater. Sci.* **2018**, *53*, 7621–7636. [[CrossRef](#)]
20. Huang, T.; Cui, W.; Qiu, Z.; Hu, Z.; Zhang, Z. 2D porous layered NiFe_2O_4 by a facile hydrothermal method for asymmetric supercapacitor. *Ionics* **2021**, *27*, 1347–1355. [[CrossRef](#)]
21. Zhang, X.; Zhu, M.; Ouyang, T.; Chen, Y.; Yan, J.; Zhu, K.; Ye, K.; Wang, G.; Cheng, K.; Cao, D. NiFe_2O_4 nanocubes anchored on reduced graphene oxide cryogel to achieve a 1.8 V flexible solid-state symmetric supercapacitor. *Chem. Eng. J.* **2019**, *360*, 171–179. [[CrossRef](#)]
22. Javed, M.S.; Zhang, C.; Chen, L.; Xi, Y.; Hu, C. Hierarchical mesoporous NiFe_2O_4 nanocone forest directly growing on carbon textile for high performance flexible supercapacitors. *J. Mater. Chem. A* **2016**, *4*, 8851–8859. [[CrossRef](#)]
23. Hareesh, K.; Shateesh, B.; Joshi, R.P.; Dahiwale, S.S.; Bhoraskar, V.N.; Haram, S.K.; Dhole, S.D. PEDOT:PSS wrapped $\text{NiFe}_2\text{O}_4/\text{rGO}$ tertiary nanocomposite for the super-capacitor applications. *Electrochim. Acta* **2016**, *201*, 106–116. [[CrossRef](#)]
24. Chang, Z.; Li, T.; Li, G.; Wang, K. One-pot in-situ synthesis of $\text{Ni(OH)}_2\text{-NiFe}_2\text{O}_4$ nanosheet arrays on nickel foam as binder-free electrodes for supercapacitors. *J. Mater. Sci. Mater. Electron.* **2018**, *30*, 600–608. [[CrossRef](#)]
25. Scindia, S.S.; Kamble, R.B.; Kher, J.A. Nickel ferrite/polypyrrole core-shell composite as an efficient electrode material for high-performance supercapacitor. *AIP Adv.* **2019**, *9*, 055218. [[CrossRef](#)]
26. Chen, R.; Yu, M.; Sahu, R.P.; Puri, I.K.; Zhitomirsky, I. The development of pseudocapacitor electrodes and devices with high active mass loading. *Adv. Energy Mater.* **2020**, *10*, 1903848. [[CrossRef](#)]
27. Kinemuchi, Y.; Ishizaka, K.; Suematsu, H.; Jiang, W.; Yatsui, K. Magnetic properties of nanosize NiFe_2O_4 particles synthesized by pulsed wire discharge. *Thin Solid Film.* **2002**, *407*, 109–113. [[CrossRef](#)]
28. Tien, N.A.; Mittova, V.; Sladkopevtsev, B.; Mai, V.Q.; Mittova, I.Y.; Vuong, B.X. Structural, optical and magnetic properties of Y-doped NiFe_2O_4 nanoparticles prepared by simple co-precipitation method. *Solid State Sci.* **2023**, *138*, 107149. [[CrossRef](#)]

29. Bashir, A.; Matinise, N.; Sackey, J.; Kaviyarasu, K.; Madiba, I.; Kodseti, L.; Ezema, F.; Maaza, M. Investigation of electrochemical performance, optical and magnetic properties of NiFe₂O₄ nanoparticles prepared by a green chemistry method. *Phys. E Low-Dimens. Syst. Nanostructures* **2020**, *119*, 114002. [[CrossRef](#)]
30. Dippong, T.; Cedar, O.; Levei, E.A. Effect of Transition Metal Doping on the Structural, Morphological, and Magnetic Properties of NiFe₂O₄. *Materials* **2022**, *15*, 2996. [[CrossRef](#)]
31. Reddy, R.N.; Reddy, R.G. Sol-gel MnO₂ as an electrode material for electrochemical capacitors. *J. Power Sources* **2003**, *124*, 330–337. [[CrossRef](#)]
32. Jeong, Y.; Manthiram, A. Nanocrystalline manganese oxides for electrochemical capacitors with neutral electrolytes. *J. Electrochem. Soc.* **2002**, *149*, A1419. [[CrossRef](#)]
33. Dong, W.; Sakamoto, J.S.; Dunn, B. Electrochemical properties of vanadium oxide aerogels. *Sci. Technol. Adv. Mater.* **2003**, *4*, 3–11. [[CrossRef](#)]
34. Tallman, D.; Vang, C.; Wallace, G.; Bierwagen, G. Direct electrodeposition of polypyrrole on aluminum and aluminum alloy by electron transfer mediation. *J. Electrochem. Soc.* **2002**, *149*, C173. [[CrossRef](#)]
35. Chen, S.; Zhitomirsky, I. Influence of dopants and carbon nanotubes on polypyrrole electropolymerization and capacitive behavior. *Mater. Lett.* **2013**, *98*, 67–70. [[CrossRef](#)]
36. Wang, G.-L.; Xu, J.-J.; Chen, H.-Y. Dopamine sensitized nanoporous TiO₂ film on electrodes: Photoelectrochemical sensing of NADH under visible irradiation. *Biosens. Bioelectron.* **2009**, *24*, 2494–2498. [[CrossRef](#)] [[PubMed](#)]
37. Seung-Hoon, S.; Young-Je, Y. Characteristics of mediated enzymatic nitrate reduction by galloxyanine-bound nanoporous electrode. *J. Microbiol. Biotechnol.* **2006**, *16*, 505–510.
38. Snook, G.A.; Kao, P.; Best, A.S. Conducting-polymer-based supercapacitor devices and electrodes. *J. Power Sources* **2011**, *196*, 1–12. [[CrossRef](#)]
39. Raudsepp, T.; Marandi, M.; Tamm, T.; Sammelselg, V.; Tamm, J. Influence of ion-exchange on the electrochemical properties of polypyrrole films. *Electrochim. Acta* **2014**, *122*, 79–86. [[CrossRef](#)]
40. Sikkema, R.; Zhitomirsky, I. Magnetic supercapacitors: Charge storage mechanisms, magnetocapacitance, and magnetoelectric phenomena. *Appl. Phys. Rev.* **2023**, *10*, 021307. [[CrossRef](#)]
41. Wang, Y.; Liu, Y.; Zhitomirsky, I. Surface modification of MnO₂ and carbon nanotubes using organic dyes for nanotechnology of electrochemical supercapacitors. *J. Mater. Chem. A* **2013**, *1*, 12519–12526. [[CrossRef](#)]
42. Shrikrushna, S.; Kher, J.A.; Kulkarni, M.V. Influence of dodecylbenzene sulfonic acid doping on structural, morphological, electrical and optical properties on polypyrrole/3C-SiC nanocomposites. *J. Nanomed. Nanotechnol.* **2015**, *6*, 1. [[CrossRef](#)]
43. Hu, J.; Li, Y.; Gao, G.; Xia, S. A mediated BOD biosensor based on immobilized *B. subtilis* on three-dimensional porous graphene-polypyrrole composite. *Sensors* **2017**, *17*, 2594. [[CrossRef](#)] [[PubMed](#)]

Disclaimer/Publisher's Note: The statements, opinions and data contained in all publications are solely those of the individual author(s) and contributor(s) and not of MDPI and/or the editor(s). MDPI and/or the editor(s) disclaim responsibility for any injury to people or property resulting from any ideas, methods, instructions or products referred to in the content.